



# Effect of the mask geometry on the microstructure forming in through-mask electrochemical micromachining

Guoqian Wang<sup>1</sup> · Shan Jiang<sup>1</sup> · Shoudong Ni<sup>1</sup> · Yan Zhang<sup>1</sup>

Received: 26 October 2022 / Accepted: 20 March 2023 / Published online: 31 March 2023  
© The Author(s), under exclusive licence to Springer-Verlag London Ltd., part of Springer Nature 2023

## Abstract

The manufacturing of surface microstructure is an important means for the modification of surface characteristics of parts. Through-mask electrochemical manufacturing is also an efficient way to fabricate surface microstructures. Nevertheless, in cases where the through-mask electrochemical manufacturing is used for the fabrication of microstructures, many experiments are required to control the cross-section morphology of the microstructures. Furthermore, there is a lack of quantitative analysis of the impact of key variables on the process. In this paper, using numerical simulations based on the mask geometry, we analyze the effects of the aspect ratio of mask feature and the gap between cathode to mask on electrochemical micromachining. We further investigate the influence laws of the mask geometry on the anode current density distribution and forming process. A critical value of “0.8” is also determined for aspect ratio of mask feature which is closely related to the anode current density distribution and forming process. The through-mask electrochemical micromachining experiments confirm the effect laws of the geometric structure of the mask feature. And the critical value (0.8) of aspect ratio can be used as the basis for selecting mask feature.

**Keywords** Mask geometry · Forming process, Aspect ratio of mask · Current density

## 1 Introduction

In surface engineering technology, it is essential to modify the surface characteristics by preparing different array structures on the metal surfaces. This is to realize the functions of metal surfaces such as drag reduction, heat transfer enhancement, and friction reduction [1, 2]. The major preparation methods of surface microstructures include additive and subtractive manufacturing [3]. The through-mask electrochemical micromachining (TMEMM) is one of the subtractive manufacturing technologies for surface microstructure manufacturing [4, 5].

TMEMM controls the electrolytic reaction area on the anode workpiece by using an insulating mask. The mask structure is copied onto the workpiece surface by the dissolution of the anode metal in the electrochemical reaction. A unique advantage of TMEMM is its efficient micromachining process and good surface quality. Furthermore, it

does not have any hidden risks such as thermal effect, stress effect, and deformation of the workpiece after micromachining. Therefore, TMEMM is emerging as a promising prospect in the field of surface microstructure manufacturing [6]. Many researchers investigate TMEMM properties such as material removal rate, surface quality, and forming process [7, 8]. One of the common research themes on the forming process is focused on the analysis of the morphology evolution and forming accuracy of the microstructure.

Faraday’s law implies that the material removal rate in the electrolysis process depends on the current density on the material surface. Hence, different distributions of current density on the machined surface lead to different forming processes and microstructures. The factors affecting the current density include power supply parameters, electrolyte characteristics, mass transfer in the flow field, and mask geometry [9]. The impact of power supply parameters is the most straightforward. For the same processing conditions, the higher the voltage or current, the greater the current density. Nevertheless, reasonable power supply parameters are also essential. Courtney et al. presented a process to micromachine emitter array on porous metals by using electrochemical etching with photolithographic mask. And

✉ Guoqian Wang  
wangq@njtech.edu.cn

<sup>1</sup> School of Mechanical and Power Engineering, Nanjing Tech University, Nanjing 211816, China

they found that it is very important to control pulsed voltage for emitter uniformity and pore integrity [10]. Similar in fabricating micro-pillar arrays, the effects of the current density on surface morphology of the micro-pillar arrays were investigated by Sun et al. [11]. Baldhoff et al. reported that specific voltage is the key to micro-channel shape uniform during TMM on aluminum [12].

Furthermore, the efficiency of the electrolyte characteristics on the current density is mainly affected by the conductivity, passivation, and activation of the solution. Different electrolyte flow patterns will affect the product mass transfer and conductivity stability, as reported by Kunar et al. [13] and Zhao et al. [14]. The above factors mainly affect the current density, whereas the mass transfer in the flow field and the mask geometric characteristics also affect both the current density and its distribution characteristics. One of the major functions of the electrolyte flow field is to take the electrolytic products away from the micromachining region. However, lower mass transfer efficiency or uneven mass transfer rate also affect the original conductivity of the electrolyte, hence resulting in changes in the distribution of current density on the machining surface. Therefore, Wu et al. applied the jet technology to the TMM to obtain more efficient mass transfer and better dimensional symmetry [15]. Chen et al. set the mask on the cathode of jet electrochemical machining, which significantly improving the mass transfer efficiency and processing flexibility [16]. In addition to changing the flow patterns, Zhai et al. found that the megasonic wave agitation can improve the electrolysis process so as to enhance the deep etching by approximately 57% relative to traditional TMM [17]. It was shown that strengthening the mass transfer efficiency and improving the mass transfer uniformity of the flow field can eliminate the mass transfer effect of the flow field on the current density.

In TMM, the effect of the geometric structure of mask feature on the current density is also unique. The main function of the mask is to control the electrolytic reaction region and to ensure the accuracy of microstructure forming. Kunar et al. covered the photolithographic mask on the cathode surface to obtain reusable mask tool, which reduced the cost and preparation time [18]. In order to promote the processing localization, Chen et al. designed the masked porous cathode and jet flow mode to achieve a contact processing of TMM [19]. Although contact TMM improves the localization, it reduces the mass transfer efficiency. Therefore, Zhao et al. tried to heighten the mass transfer efficiency by the magnetic field force and linear reciprocation, and got up certain results [20]. Furthermore, the shielding and limiting effect of the mask on the electric field directly affects the magnitude and distribution of the current density. Mahata et al. utilized low-aspect ratio mask to get higher current density and more efficient processing in fabricating micro-dimple array by TMM [21]. The highly effective flexible

cathode was proposed by Patel et al. and applied to fabricate micro-structures on various curved surfaces [22].

The existing research works also demonstrate a strong regularity of the effect of mask geometry on the current density; nevertheless, a quantitative analysis of the relevant laws is still lacking. Systematically analysis of the influence of the geometric parameters on the current density and finding out the important quantitative values enable predicting/controlling the forming process in TMM by designing the mask geometric structure.

## 2 Physical model and conditions for numerical simulation

The process of TMM is illustrated in Fig. 1a. The electrolytic reaction region is composed of a cathode, an anode, and an insulating mask. After reasonable simplification of the electrolytic reaction region, the geometric model for numerical simulation is constructed as shown in Fig. 1b. The main boundaries include the cathode boundary  $\Gamma_1$ , anode boundary  $\Gamma_2$ , the side wall of the insulating board ( $\Gamma_3$  and  $\Gamma_4$ ), and the virtual boundary of electrolyte ( $\Gamma_5$  and  $\Gamma_6$ ).

In the simulation process, the electric field distribution is calculated according to the Laplace equation, and the material removal process is obtained based on Ohm's and Faraday's laws. In this work, analyze the effect of geometric parameters among the cathode, mask, and anode on the electric field distribution and anode forming process will be analyzed, mainly including the gap between cathode and mask ( $a$ ), the opening width of the mask pattern structure ( $d$ ) (also to referred as the "mask pattern width"), and the thickness of mask ( $h$ ) which is the depth of mask pattern structure (also referred to as "mask pattern depth"). Among these parameters, there is a correlation between the effect of mask pattern width and mask thickness, which can be attributed to the parameter called "aspect ratio ( $AR$ ) of mask feature." This parameter denotes the ratio of the mask pattern depth to its width (i.e.,  $AR = h/d$ ). The value range of the above geometric parameters is shown in Table 1 where there are a total of 3364 combinations of geometric parameters.

According to the above electric field model and geometric characteristics, the COMSOL software was used to simulate and calculate the geometric parameter combinations in a parametric scanning mode. We also analyze the electric field intensity distribution in the mask electrochemical machining area as well as the anode forming process. During the simulation process, except for the geometric parameters, all parameters remain unchanged. For easy the simulation process, the current efficiency of the material is assumed to be 100%, and the other processing and material parameters are presented in Table 2.

**Fig. 1** Model of numerical simulation: **a** illustration of TMEMM; **b** geometric model for numerical simulation

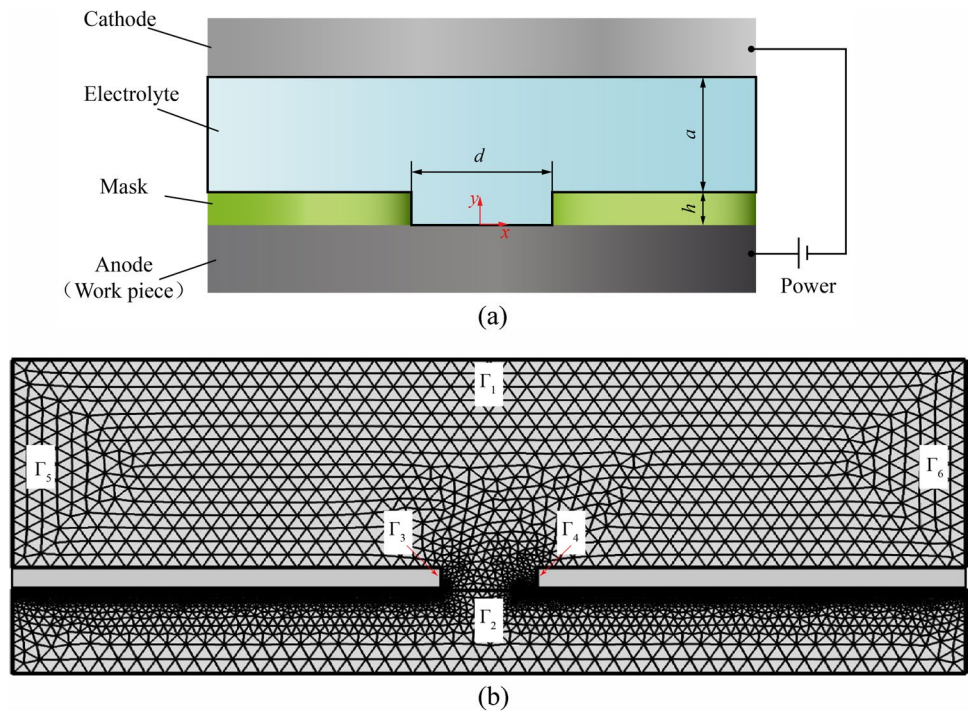


**Table 1** The value range of the geometric parameters

Geometric parameters	Value range
Mask pattern width, $d$ , mm	0.05, 0.2, 0.5, 1
Aspect ratio of mask feature, $AR$	0.1~2.0, step-size 0.1
Gap between cathode and mask, $a$ , mm	0.001~0.009, step-size 0.001 0.01~0.09, step-size 0.01 0.1~2.0, step-size 0.1

**Table 2** Simulation conditions

Parameters	Values
Processing voltage $U$ (V)	30
Electrolyte conductivity $\sigma$ ( $\Omega^{-1}\cdot\text{m}^{-1}$ )	7.9
Time step $\Delta t$ (s)	0.2
Processing time $T$ (s)	60

### 3 Analysis of simulation results

In the process of TMEMM, the current density on the anode surface determines the material removal rate. The removal rates of the machined surface are also directly associated with the variation of the anode surface morphology. Also, the change of anode surface morphology results in different gaps between the anode and cathode, affecting the anode surface current density. Therefore, the variation of anode surface morphology and current density distribution are interactively related and dynamically change.

In the following sections, the effect of geometric structure on the initial current density distribution is analyzed. We then discuss the critical geometric parameters affecting the initial current density distribution characteristics. Finally, we elaborate on the TMEMM anode forming principle.

#### 3.1 Effect of the gap between the cathode and mask on the initial current density

The initial current density distribution determines the initial morphology of the anode and has a decisive influence on the anode forming process. To compare the changes in current density distribution, the normalized difference ( $ND$ ) of current density is introduced as a reference value. It is defined as the ratio of the difference between the current density at each point of the anode to the minimum and minimum current densities:

$$ND = \frac{N_i - N_{\min}}{N_{\min}}$$

where  $N_i$  is the current density at point  $i$  and  $N_{\min}$  denotes the minimum current density on the anode surface. The closer the normalized difference to 0, the more consistent the current density distribution.

Figure 2 shows the effect of different gaps between the cathode and mask on the initial current density, where the mask thickness and its width are fixed. It is seen that the initial current density gradually increases with the decrease of the gap between the cathode and mask.

**Fig. 2** Effect of different gaps between the cathode and mask on the initial current density: **a** change of current density value; **b** normalized difference of current density

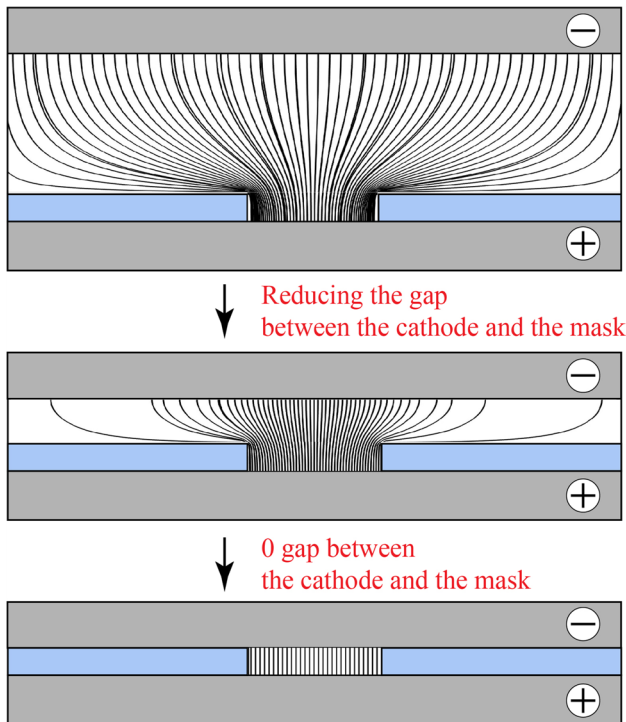
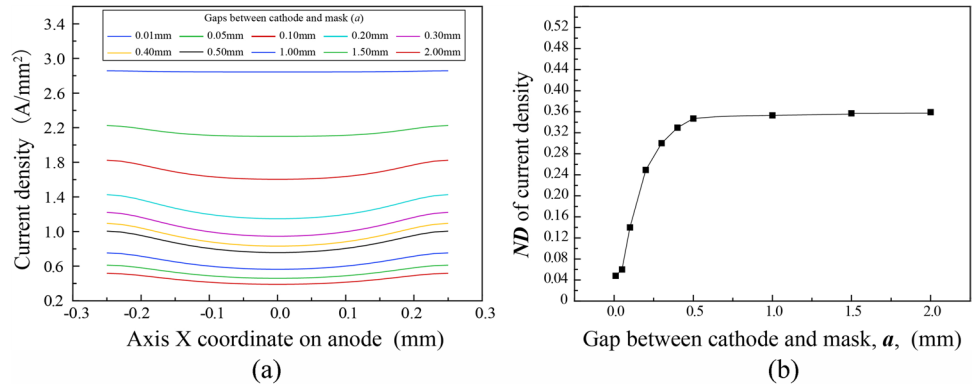


**Fig. 3** Change in the binding force of the mask on the electric field

Furthermore, the normalized difference of current density gradually approaches zero, indicating that the distribution of current density tends to be consistent by increasing the gap. The increase in current density is attributed to the increasing current density caused by decreasing the gap that reduces the distance between the cathode and the anode.

The change in the current density distribution is due to the change in the binding force of the mask on the electric field. Figure 3 shows that by reducing the gap between the cathode and the mask, the current line in the mask hollow region becomes more concentrated. Nevertheless, it is more difficult to affect the anode current density above the masking area. Therefore, by increasing the gap

between the cathode and the mask, the electric field in this area might impose a greater impact. This then significantly increases the current density at the edge of the mask structure compared to that of the center. By decreasing the gap, the electric field is increasingly confined in the mask structure, and the current density tends to be more consistent.

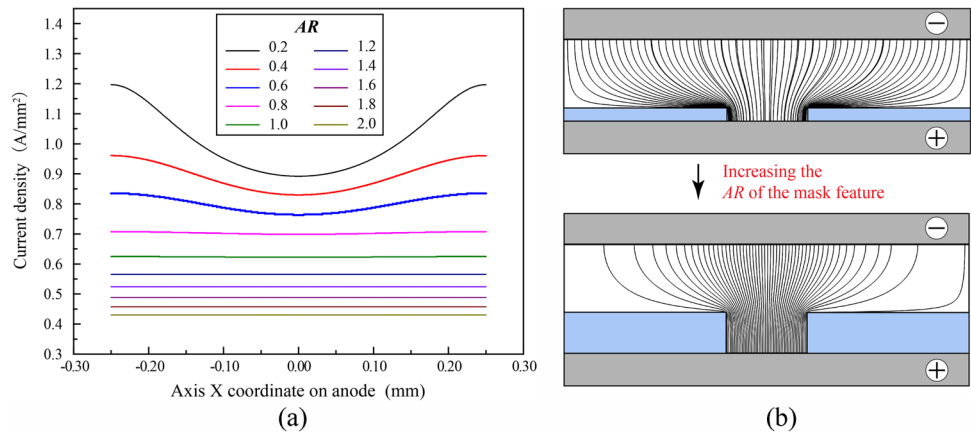
For a “0” gap between the cathode and the mask, the current density becomes completely consistent. This state has been used in industrial engineering [23]. However, the disappearance of the gap between the cathode and mask could challenge renewing the electrolyte and the continuity of the material processing. A consistent current density while ensuring a certain distance is therefore favorable. To further investigate this, in the following, we analyze the effect of the aspect ratio (*AR*) of mask feature on the initial current density.

### 3.2 Effect of *AR* of mask feature on initial current density

Figure 4 shows the effect of the *AR* of mask feature on the initial current density. Regardless of the distance between the cathode and the mask, the initial current density distribution tends to be consistent with the increase of *AR* value and the current density gradually decreases. The reason is the enhancement of the binding force of the mask in the electric field. Figure 4 b shows that for a small *AR* of mask feature, the mask cannot effectively constrain the electric field effect in the mask region. Also, the current density at the edge of the hollow area is higher than that of the center. As the mask thickness increases, Fig. 4b shows that the stronger the masking effect on the electric field in the mask area, the greater the elimination of the concentration of current density at the edge of the hollow area. This results in a consistent current density. Therefore, increasing the value of *AR* of mask feature also results in a consistent current density distribution while ensuring sufficient spacing for the electrolyte renewal.



**Fig. 4** Effect of the AR of mask feature on the initial current density: **a** change of current density value; **b** change in the binding force of the AR on the electric field



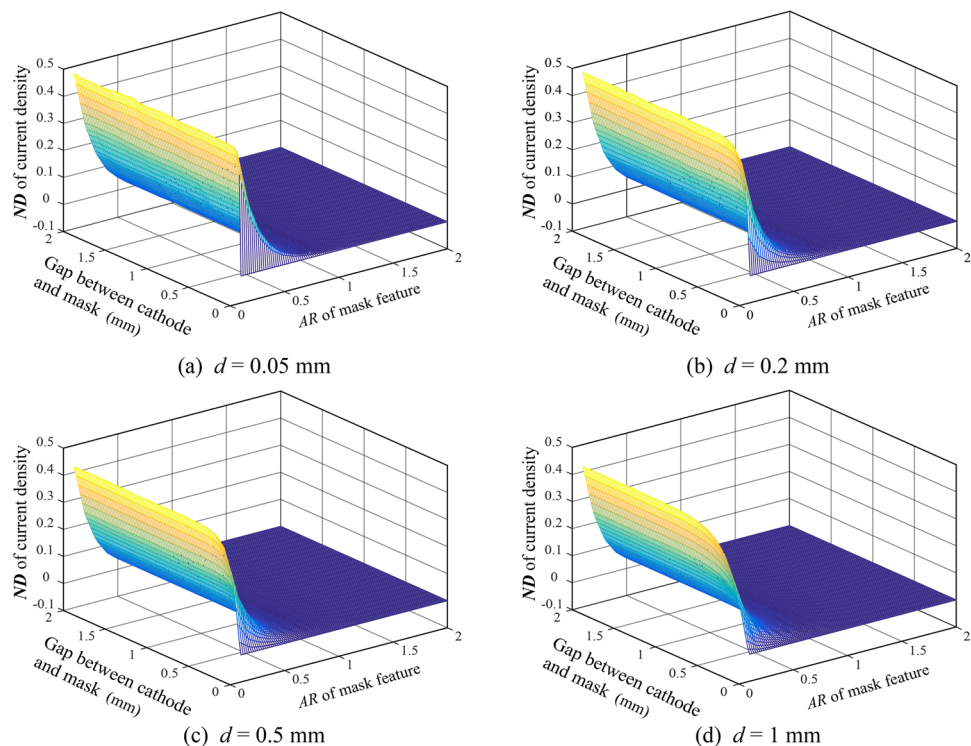
### 3.3 Critical geometric parameters of the initial current density distribution

The previous analysis shows that both the gap between the cathode and mask and the AR of mask feature affect the initial current density. The distribution surface shown in Fig. 5 can be therefore obtained by considering both of the effects. The results show that the distribution of the current density tends to be uniform with the decrease of the gap between the cathode and mask. And the distribution of the current density also tends to be uniform with the increase of the AR of mask feature. Further analysis of the interactions between the two factors shows that for a

small gap between the cathode and mask, by changing the AR of mask feature, the normalized difference of current density is insignificant.

Moreover, for a large AR of mask feature, the normalized difference of current density no longer change with the change of the gap between the cathode and mask. Furthermore, the effect of AR on the normalized difference of current density becomes more consistent by comparing the variation trend of surfaces with different mask pattern widths. Note that the effect of the distance between the cathode and mask on the normalized difference of current density is different under various mask pattern widths. Compared to Fig. 5 a and d, where the mask pattern width

**Fig. 5** Initial current density by considering both the gap between the cathode and mask and the AR of mask feature



is 0.05 mm and the gap between the cathode and mask is less than 0.1 mm, the normalized difference in current density is significantly decreased. For a 1-mm width of the mask, with a gap between the cathode and mask lower than 0.8 mm, the normalized difference of current density is also significantly decreased. These results show that to obtain uniform current density distribution, a smaller mask pattern width requires a smaller distance between the cathode and mask.

For further quantitative analysis, a normalized difference of current density needs to be given as the critical value to obtain the corresponding values of the gap between the cathode to mask and the *AR* of mask feature. In the real electrochemical machining process, when the normalized difference of current density on the anode surface reaches 0.01, the distribution of current density becomes uniform. Therefore, the critical value (“0.01”) of the normalized difference of current density is set for screening the calculation results.

Table 3 presents the combination of the gap between the cathode and mask and the *AR* of mask feature resulting in a normalized difference in the current density (0.01) on the anode surface. Comparing the data, it is further seen that the smaller the mask pattern width, the smaller the gap required between the cathode and mask to obtain a uniform current density. The smaller the aspect ratio of the mask feature, the smaller the gap between the cathode and the mask is required to obtain uniform current density. For instance, for a mask pattern width of 0.05 mm and the *AR* of mask feature of 0.1, the distance between the cathode and mask needs to be less than or equal to 0.001 mm. This enables the anode surface to achieve a uniform current density distribution. However, when the mask pattern width is 1 mm and the *AR* of mask feature is the same, a uniform current density distribution is obtained on the anode surface. In this case, the required distance between the cathode and the mask is only 0.01 mm. In Table 3, there is an important node in the *AR* of mask feature, where the *AR* of mask feature is 0.8, a uniform current density distribution is achieved, and the required distance between the cathode and the mask is 2 mm.

Comparing the *AR* of mask feature of 0.7 and 0.8, the corresponding gap between the cathode and mask is rather abrupt indicating that homogenization of anode surface current density distribution in this range. Therefore, the value of 0.8 is an important node value of the *AR* of mask feature. The significance of the value is for a small mask pattern width; it is difficult to obtain a uniform current density distribution by adjusting the gap between the cathode and the mask. Therefore, a uniform current density distribution can be obtained through this *AR* of mask feature. Even for a small mask pattern width, the aspect ratio

**Table 3** Node values of key parameters

Width of mask feature (mm)	<i>AR</i> of mask feature	Gap between the cathode and mask (mm)	Normalized difference of current density
0.05	0.1	0.001	0.0105
	0.2	0.001	0.0046
	0.3	0.002	0.0069
	0.4	0.003	0.0068
	0.5	0.005	0.0078
	0.6	0.009	0.0089
	0.7	0.02	0.0092
	0.8	2	0.0082
0.2	0.1	0.003	0.0095
	0.2	0.006	0.0092
	0.3	0.01	0.0099
	0.4	0.01	0.0051
	0.5	0.02	0.0079
	0.6	0.03	0.0072
	0.7	0.09	0.0098
	0.8	2	0.0073
0.5	0.1	0.007	0.0084
	0.2	0.01	0.0045
	0.3	0.02	0.0069
	0.4	0.03	0.0068
	0.5	0.05	0.0078
	0.6	0.1	0.0099
	0.7	0.2	0.0090
	0.8	2	0.0060
1	0.1	0.01	0.0048
	0.2	0.03	0.0091
	0.3	0.05	0.0098
	0.4	0.07	0.0087
	0.5	0.1	0.0079
	0.6	0.2	0.0099
	0.7	0.5	0.0099
	0.8	2	0.0060

value of the mask feature can be used as an important mask structure selection standard.

### 3.4 Analysis of anode forming process

Analyzing the relationship between mask feature and initial current density shows that mask feature with different *AR* results in different initial current density distributions. The initial current density distribution also affects the formation of subsequent anodes. Here, we investigate the forming of anode under various initial current densities.

As an example, we consider the mask feature width of 0.05 mm and the anode-cathode spacing of 1 mm and simulate the forming process of mask feature with different

**Table 4** Normalized difference of initial current at different ARs of mask feature

AR of mask feature	Normalized difference of initial current density
0.2	0.2344
0.5	0.0385
0.8	0.0059
2	0

aspect ratios. Table 4 presents four selected ARs of mask feature and the corresponding normalized difference of initial current density.

The cross-section morphology of the anode at different processing times can be calculated using the mathematical model of anodic dissolution in mask electrochemical micromachining. This is then used to analyze the forming principles of the anode. Figure 6 shows the calculated variation curve of anode section morphology at different processing times. The change of anode cross-section morphology at the AR of mask feature of 0.2 and the normalized difference of initial current density of 0.2344 is presented in Fig. 6a. It is seen that the normalized difference of current density at the initial moment of the anode is rather large. The distribution of current density is also higher at the edge and lower at the center. Therefore, the anode

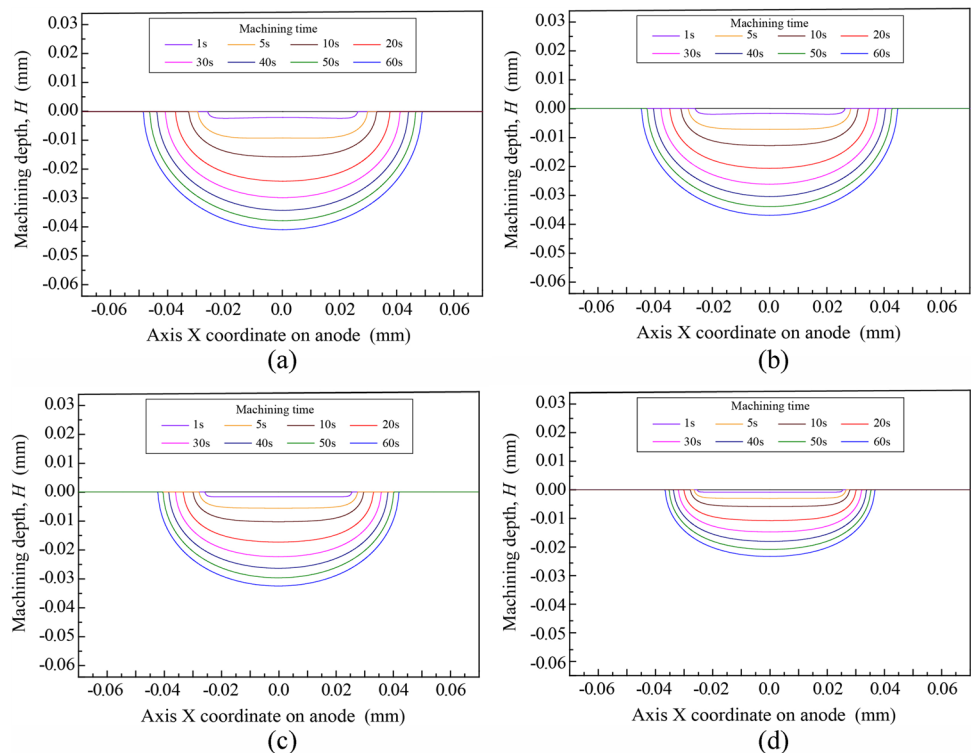
cross-section morphology obtained after processing for 1 s has a “hump” morphology with a bulge in the center.

As the processing goes on, the central bulge is gradually eliminated. For the processing time of 10 s, the anode section forms a flat-bottomed pit. By further increasing the processing time, the anode section morphology gradually forms arc-shaped pits. By increasing the aspect ratio to 0.5, the normalized difference of the initial anode current density decreases to 0.0385.

The changes in the anode section morphology are also shown in Fig. 6b. The process follows the same trend as the case where the aspect ratio is 0.2. However, for a processing time of 1, since the normalized difference of the initial current density decreases, the bulge of the anode section center is smaller. At the same time, when the processing time is 5 s, the anode section formed a flat-bottomed pit. With the increase of time, the anode section morphology gradually forms an arc-shaped pit. Figure 6 c and d show the changes of the anode cross-section morphology for AR of mask feature of 0.8 and 2, respectively.

Since the normalized difference of the current density at the initial time of the anode is less than 0.01, the distribution of current density is uniform. Therefore, there is no central convex cross-section morphology during the processing. However, it directly changes from a flat-bottomed pit to an arc-shaped pit. By comparing the electrochemical corrosion depth of the anode surface at the same time under different aspect ratios, it is also seen that the smaller the AR of mask

**Fig. 6** The change of anode cross-section morphology at different ARs of mask feature: **a** AR = 0.2; **b** AR = 0.5; **c** AR = 0.8; **d** AR = 2



feature, the greater the corrosion depth of the anode surface at the same processing time.

The physical model of the electric field during the mask electrochemical micromachining also implies that the current needs to pass through the mask pattern. It is then transmitted from the anode to the cathode. The mask structure with a high aspect ratio can effectively constrain the electric field distribution on the anode surface. With the increase of the  $AR$  of mask feature, the shielding of the mask to the electric field also increases; hence, the electric field strength on the anode surface gradually decreases. It is also seen that increasing the aspect ratio of the mask structure reduces the efficiency of ECM.

The change process of anode cross-section morphology with different aspect ratios also indicates that in TMEMM, the changes of anode cross-section morphology can be divided into two categories. For normalized differences ( $ND$ ) of the initial current density greater than 0.01, the variation process of the cross-section morphology of the anode is shown in Fig. 7a. As seen, it develops from a convex cross-section to a flat-bottom cross-section, and finally forms an arc cross-section.

In cases where the normalized difference of initial current density  $ND$  is lower than 0.01, the variation process of anode section morphology is shown in Fig. 7b. As seen, it changes from a flat bottom section to a circular arc section. In practical engineering applications, different initial current densities can be obtained by changing the  $AR$  of mask feature. According to the above analysis, when the  $AR$  of mask feature is no less than 0.8, the normalized difference of anode initial current density can be less than 0.01. If a larger normalized difference of current density is required, a smaller  $AR$  of mask feature can be selected. Therefore, a reasonable mask structure can be selected according to the processing requirements.

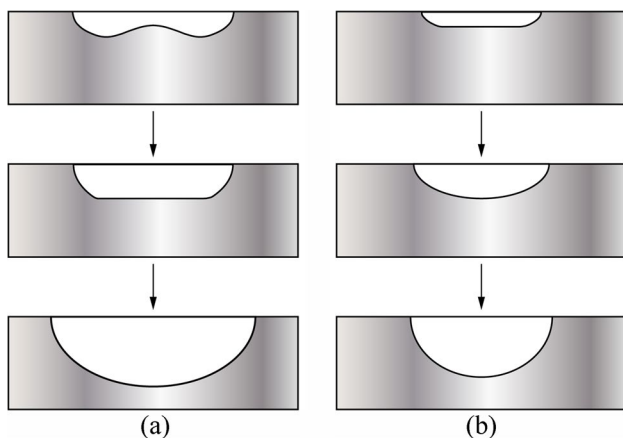


**Fig. 7** The variation process of anode section morphology: **a**  $AR < 0.8$ ; **b**  $AR \geq 0.8$

To quantitatively analyze the material removal principle of the anode in TMEMM, the etch factor ( $EF$ ) is introduced. In TMEMM, the material removal on the anode surface occurs simultaneously in different directions. There exists axial corrosion in the  $Y$ -axis direction and lateral corrosion in the  $X$ -axis direction. The ratio of the two etching depths is the etching factor  $EF$ . In other words,  $EF$  represents the mask electrolysis processing rule under different mask and processing conditions. The equation of etching factor ( $EF$ ) is:

$$EF = \frac{2H}{D - d}$$

where  $H$  is the corrosion depth in the  $Y$ -axis direction,  $D$  denotes the width or diameter of the processed structure, and  $d$  is the width or diameter of the mask structure. The difference between the two values is the lateral corrosion width in the  $X$ -axis direction.

Figure 8 shows the anodic etching factor  $EF$  versus time for four different  $AR$ s of mask feature. It is seen that the anodic etching factor gradually decreases with the extension of processing time regardless of the mask depth width ratio. This indicates that with the increase in processing time, the axial etching factor of the anode is decreased and the lateral etching factor is accelerated. At a certain time, the anodic etching factor becomes stable. With the progress of processing, the gap between the anode and cathode gradually increases, and the current density on the anode surface tends to be consistent.

The curves of anodic etching factor under different  $AR$ s of mask feature are compared horizontally. As seen, at the same processing time, the larger the  $AR$  of mask feature, the higher the anodic removal ratio is. For  $AR$ s of mask feature equal to 0.2 and 0.5, at the processing time

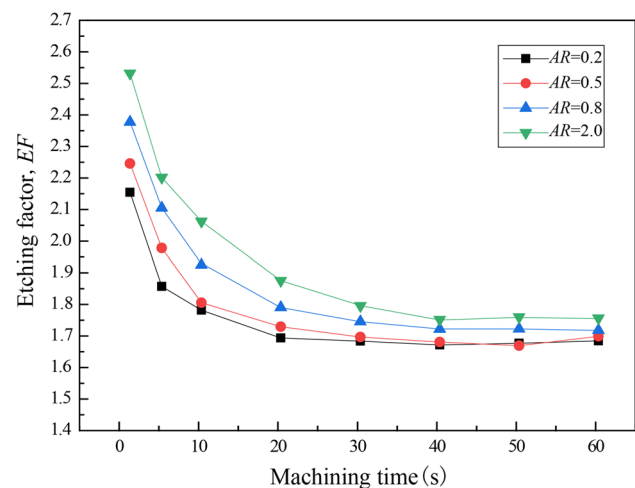


**Fig. 8** Anodic etching factor  $EF$  versus time for four different  $AR$ s of mask feature



of 20 s, the anodic etching does not change. For the AR of mask feature equal to 0.8, the anodic etching becomes stable after 30 s. For the AR of mask feature equal to 2, the anodic removal etching reaching becomes stable after 40 s. These results show that a larger AR of mask feature can effectively strengthen the corrosion in the anode depth direction while constraining the lateral corrosion. By analyzing the etch factor of TMEMM, it is also seen that even for a large AR of mask feature, it is difficult to machine a structure with an aspect ratio greater than 1. Therefore, TMEMM is mostly used to process metal array structures with small aspect ratios.

By analyzing the anode forming process under different mask structures, it is found that the normalized difference of anode initial current density is different due to different AR of mask feature. This results in two types of

anode-forming processes in TMEMM. Furthermore, the larger the AR of mask feature, the higher the anode etching factor in TMEMM. However, the anode etching factor always decreases gradually with the processing time. As a result, TMEMM is more suitable for the processing of array structures with small aspect ratios.

### 4 Experiments

To verify the accuracy of the numerical simulation, the TMEMM experiment of micro-pits is designed. In the experiment, the mask structure with array-hole is used to process the pits on the anode. The diameter of the mask hole is 50 μm. By changing the thickness of the mask, the different combinations of aspect ratio are formed; the values are shown in Table 5. The changes in current and anode morphology in the experiment are also analyzed to verify the accuracy of the simulation. Note that the material of anode is SUS 304, and the electrolyte is 10% NaNO<sub>3</sub> solution. The other experimental conditions are consistent with the simulation conditions.

The experimental results are analyzed using a laser confocal microscope and a scanning electron microscope. The laser confocal fiber is used to measure the diameter, depth, and profile of the micro-pits, whereas the scanning electron microscope is used to observe the overall surface morphology of the whole array of the micro-pits.

**Table 5** Mask geometric parameters and AR of mask feature

Mask thickness (μm)	Mask hole diameter (μm)	AR of mask feature
10	50	0.2
25	50	0.5
40	50	0.8
100	50	2

**Fig. 9** Fabrication of anode cross-section at different ARs of mask feature: **a** AR = 0.2; **b** AR = 0.5; **c** AR = 0.8; **d** AR = 2

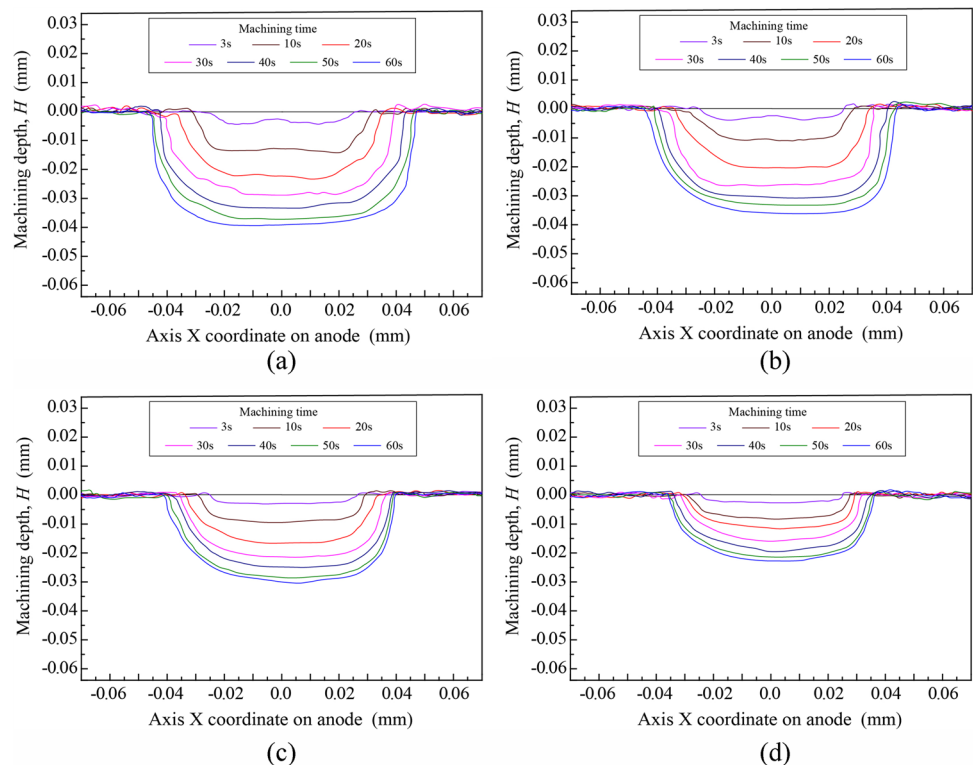
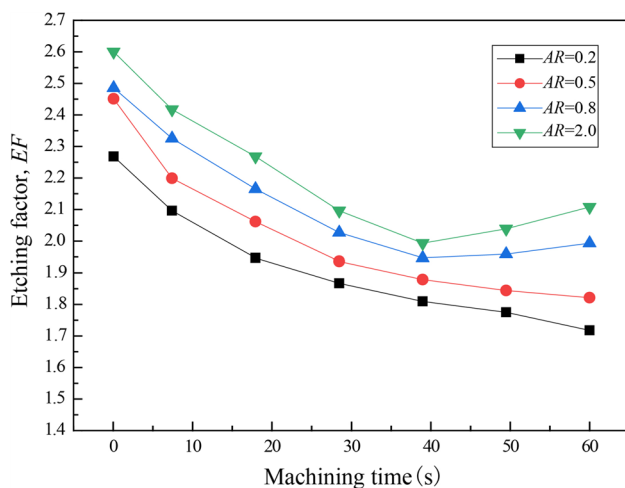


Figure 9 shows the cross-section curve of micro-pits measured by laser confocal focusing. Since after 1 s the processing depth processing is too small, the contour curve obtained using the confocal measurement is irregularly wavy. This might be attributed to the limited resolution of the confocal microscope. Therefore, the measuring nodes of processing time are adjusted to 3 s, 10 s, 20 s, 30 s, 40 s, 50 s, and 60 s. The results show that the variation trend of the microgroove section with a different  $AR$  of mask feature is almost consistent with that of simulation, but the etching rate of materials in different directions has changed. In the simulation results, with the progress of processing, the gap between cathode and anode gradually increases while the material etching rate gradually decreases, where the decrease keeps the same proportion in the axial direction and the lateral direction. In a real machining process, however, the material etching rate decreases more, especially when the aspect ratio is greater than 0.5. As the processing time increases from 40 to 50 s, the axial etching amount only increases about 1–2  $\mu\text{m}$ , i.e., the processing almost stops.

This is because in real processing, the current efficiency of SUS304 sharply drops by dropping the current density and the material etching rate reaches zero [24]. This is also seen in the radial etching rate of the anode. In the simulation results, although the radial etching rate is lower than the axial etch rate, the etching amount always exists. As shown in Fig. 6, the radial etching rate is almost constant after 20 s of machining. However, in the real processing, the radial etching is maintained at a high rate in the first 20 s and then rapidly decreased after 20 s. Due to the rapid decrease of current density, the current efficiency becomes close to 0, 40, to 60 s. The material etching amount becomes very small and tends to be 0.



**Fig. 10** Anodic etching factor  $EF$  versus time for four different  $AR$ s of mask feature

The etching factor can be also used to quantify the machining process. Figure 10 shows the etching factor in real machining. It is seen that although the basic trend is consistent with the simulation, the etching factor of templates with large aspect ratios is significantly higher than that of those with small aspect ratios. In particular, the etching factor in real machining is higher than in the simulation, the lateral material removal rate is slower in actual machining. This is because the mask not only shields the electric field, but also weakens the mass transfer process of the electrolyte flow field under the mask. Moreover, for  $AR$ s of mask feature equal to 0.2 and 0.5, the etching factor is continuously decreasing, and there is no trend similar to the simulation result that tends to be constant. For a large  $AR$  of mask feature, the etching factor is even increasing. Obviously, in the late stage of processing when the current density decreases, the etching of material tends to stop in radial direction. Thus, the aspect ratio of mask feature has a more significant impact on the change of anode morphology in actual machining.

Figure 11 shows the micro-topography of the micro-pit array processed by TMEMM with various aspect ratios after 50 s of processing. The micro-pits obtained by masks with aspect ratios of 0.2 and 0.5 are close to flat-bottomed sections, while those obtained by masks with an aspect ratio of 0.8 and 2 are circular arc sections. The three-dimensional topography in Fig. 11 is almost consistent with the two-dimensional contour in Fig. 9. Under the same processing conditions, the processing morphology can be controlled by changing the mask geometry. Furthermore, due to the decrease of current density in the final stage of machining, the machining reaches the electrolytic finishing stage, and the surface roughness of the bottom of the micro-pit is small. The surface morphology magnified to 2000 times shows that the surface structure is dense and uniform. The above results show that if a flat-bottomed pit array need be fabricated, the mask with lower aspect ratio should be used. Conversely, the mask with large aspect ratio is more suitable for fabricating an arc-bottomed micro-pits. The critical value (0.8) of  $AR$  can be used as the basis for selection. Of course, if the processing efficiency is taken into consideration, using the masks with small aspect ratios is advantageous.

The diameter ( $D$ ), depth ( $H$ ), and roughness ( $Ra$ ) of micro-pits are measured by professional instruments. All measured data are listed in Table 6. The measured data show that TMEMM has high stability. The mask with low aspect ratio can obtain larger diameter and depth, i.e., higher efficiency. Correspondingly, the mask with high aspect ratio is easier to obtain high  $EF$  and low roughness. Therefore, different mask aspect ratios can be selected when facing different processing requirements.

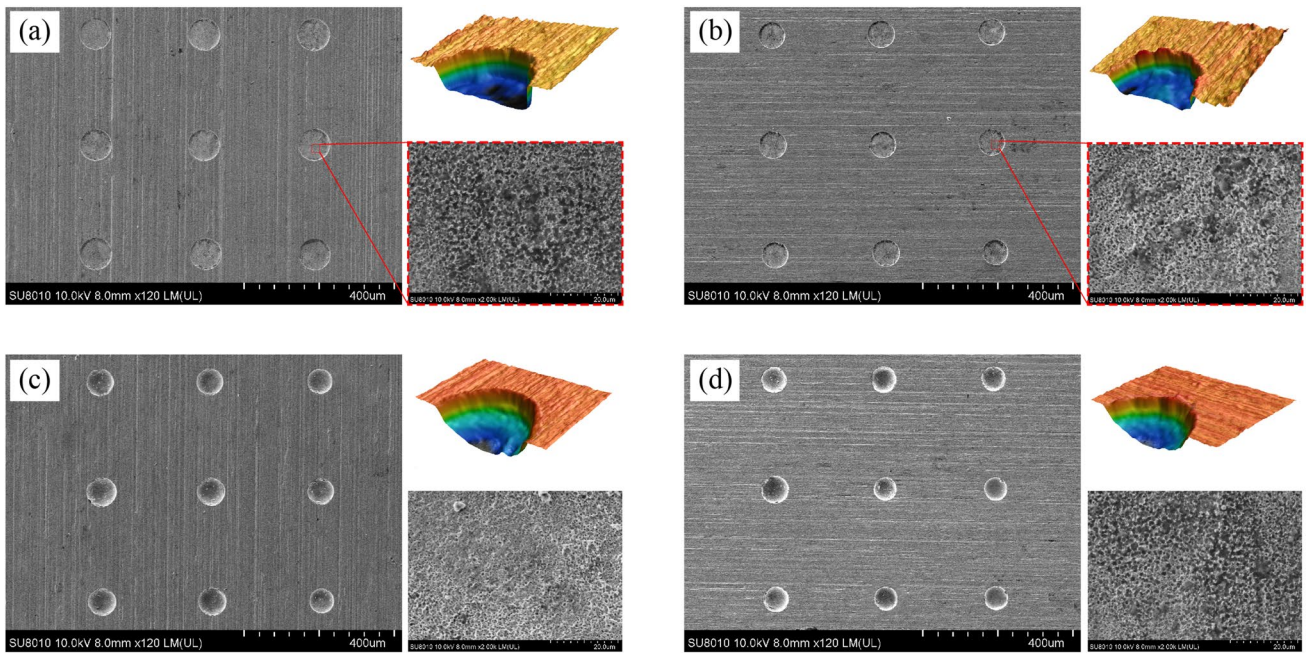


**Fig. 11** Micro-topography of the micro-pit array processed by TMEMM with various aspect ratios after 50 s of processing: **a**  $AR = 0.2$ ; **b**  $AR = 0.5$ ; **c**  $AR = 0.8$ ; **d**  $AR = 2$

**Table 6** Measurement results of micro-pits under different ARs of mask feature

ARs of mask	Measurement	Serial no.								
		1	2	3	4	5	6	7	8	9
$AR = 0.2$	$D$ ( $\mu\text{m}$ )	90.43	91.12	90.31	90.56	91.01	90.22	90.71	90.48	91.20
	$H$ ( $\mu\text{m}$ )	36.33	37.03	36.58	36.15	36.87	36.23	36.72	36.22	37.07
	$Ra$ ( $\mu\text{m}$ )	1.622	1.643	1.673	1.734	1.722	1.768	1.665	1.840	1.857
$AR = 0.5$	$D$ ( $\mu\text{m}$ )	83.16	83.51	82.79	83.59	83.91	83.48	83.84	83.44	83.13
	$H$ ( $\mu\text{m}$ )	33.58	33.98	33.22	34.03	33.76	34.14	33.84	33.73	33.92
	$Ra$ ( $\mu\text{m}$ )	1.601	1.543	1.623	1.593	1.613	1.582	1.641	1.557	1.539
$AR = 0.8$	$D$ ( $\mu\text{m}$ )	78.63	78.74	78.31	78.29	78.81	79.12	79.04	78.47	79.26
	$H$ ( $\mu\text{m}$ )	28.92	28.54	28.38	29.12	29.03	29.23	28.95	28.78	29.06
	$Ra$ ( $\mu\text{m}$ )	1.211	1.256	1.101	1.104	1.089	1.032	1.207	1.189	1.072
$AR = 2$	$D$ ( $\mu\text{m}$ )	69.89	70.25	70.43	70.18	70.33	69.85	70.06	70.18	70.24
	$H$ ( $\mu\text{m}$ )	22.94	23.64	23.41	23.22	23.15	22.87	23.37	23.16	23.32
	$Ra$ ( $\mu\text{m}$ )	0.934	0.926	0.889	0.941	0.932	0.951	0.892	0.933	0.961

### 5 Conclusions

In this paper, we use numerical analysis to investigate the geometric structures of mask feature on the efficiency of TMEMM. The aspect ratio ( $AR$ ) of the mask feature and the gap between the cathode and the mask are the most important factors of mask feature. Then, the TMEMM experiment of micro-pits is conducted. The experimental results verify the influence of mask feature on the TMEMM. The main conclusions are the following.

- 1). For any  $AR$  of mask feature, decreasing the gap between the cathode and mask improves the uniformity of the current density distribution on the anode surface. To generate a consistent current density distribution, the smaller the mask structure width and  $AR$  of mask feature, the smaller the required gap between the cathode and mask. The implementation and processing conditions are also more stringent.
- 2). The greater  $AR$  of the mask, the more consistent the anode surface current density distribution. Further-

more, for an  $AR$  of mask feature greater than or equal to a critical value of 0.8, the anode current density distribution becomes consistent regardless of the conditions of the cathode and mask gap.

- 3). It was shown that the critical value (0.8) of  $AR$  can be used as an important reference value for the design of the geometric structure of the mask. In other words, if the  $AR$  is less than 0.8, the forming process of the anode section follows a “convex section  $\rightarrow$  flat bottom section  $\rightarrow$  arc section” pattern. Also, for the  $AR$  greater than or equal to 0.8, the forming process of the anode section follows a “flat bottom section  $\rightarrow$  circular arc section” pattern.
- 4). The experimental results of TMEMM also confirm the essential impact of  $AR$  of mask feature on the current density distribution and anode forming process, and its critical value of 0.8. Given the impact of the current efficiency of material on practical processing, the results further confirm that the effect of  $AR$  of mask feature is improved. For a small aspect ratio, it is easier to obtain a flat bottom section on the anode where its curvature is smaller even for the arc-shaped surfaces. For a large aspect ratio, the anode section can quickly form an arc or even a semicircular section. This confirms that it is feasible to control the anode cross-section shape in TMEMM by taking the critical value of  $AR$  of mask feature (0.8) as a reference combined with the specific material characteristics.

**Author contribution** All authors contributed to the study conception and design. Numerical simulation and data analysis were performed by Guoqian Wang and Shan Jiang. Shoudong Ni designed the experiments. The test and analysis of experimental results were implemented by Guoqian Wang and Yan Zhang. The first draft of the manuscript was written by Guoqian Wang and Shan Jiang. All authors commented on previous versions of the manuscript. All authors read and approved the final manuscript.

**Funding** This work was supported by the National Natural Science Foundation of China (Grant No. 52205472) and the Basic Research Programs of Jiangsu (Grant No. BK20190669).

## Declarations

**Conflict of interest** The authors declare no competing interests.

## References

1. Shi G, Yu X, Meng H, Zhao F, Wang J, Jiao J, Jiang H (2022) Effect of surface modification on friction characteristics of sliding bearings: a review. *Tribol Int* 177:107937. <https://doi.org/10.1016/j.triboint.2022.107937>
2. Chu H, Xu N, Yu X, Jiang H, Ma W, Qiao F (2022) Review of surface modification in pool boiling application: coating manufacturing process and heat transfer enhancement mechanism. *Appl Therm Eng* 215:119041. <https://doi.org/10.1016/j.applthermaleng.2022.119041>
3. Brinksmeier E, Karpuschewski B, Yan J, Schönemann L (2020) Manufacturing of multiscale structured surfaces. *CIRP Ann-Manuf Techn* 69(2):717–739. <https://doi.org/10.1016/j.cirp.2020.06.001>
4. Holstein N, Krauss W, Konys J, Heuer S, Weber T (2016) Advanced electrochemical machining (ECM) for tungsten surface micro-structuring in blanket applications. *Fusion Eng Des* 109:956–960. <https://doi.org/10.1016/j.fusengdes.2016.01.045>
5. Zhai K, Du L, Wang S, Wen Y, Liu J (2020) Research on the synergistic effect of megasonic and particles in through mask electrochemical etching process. *Electrochim Acta* 364:137300. <https://doi.org/10.1016/j.electacta.2020.137300>
6. Saxena KK, Qian J, Reynaerts D (2018) A review on process capabilities of electrochemical micromachining and its hybrid variants. *Int J Mach Tool Manu* 127:28–56. <https://doi.org/10.1016/j.ijmactools.2018.01.004>
7. Wang G, Zhang Y, Li H, Tang J (2020) Ultrasound-assisted through-mask electrochemical machining of hole arrays in ODS superalloy. *Materials* 13(24):5780. <https://doi.org/10.3390/ma13245780>
8. Zou H, Yue X, Luo H, Liu B, Zhang S (2020) Electrochemical micromachining of micro hole using micro drill with non-conductive mask on the machined surface. *J Manuf Process* 59:366–377. <https://doi.org/10.1016/j.jmapro.2020.09.077>
9. Baldhoff T, Nock V, Marshall AT (2018) Review: Through-mask electrochemical micromachining. *J Electrochem Soc* 165(16):E841. <https://doi.org/10.1149/2.1341814jes>
10. Courtney DG, Li H, Lozano PC (2012) Electrochemical micromachining on porous nickel for arrays of electrospray ion emitters. *J Microelectromech S* 22(2):471–482. <https://doi.org/10.1109/jmems.2012.2227951>
11. Sun Y, Ling S, Zhao D, Liu J, Liu Z, Song J (2020) Through-mask electrochemical micromachining of micro pillar arrays on aluminum. *Surf Coat Tech* 401:126277. <https://doi.org/10.1016/j.surfcoat.2020.126277>
12. Baldhoff T, Nock V, Marshall AT (2017) Through-mask electrochemical micromachining of aluminum in phosphoric acid. *J Electrochem Soc* 164(9):E194–E202. <https://doi.org/10.1149/2.0441709jes>
13. Kunar S, Bhattacharyya B (2018) Influence of various flow methods during fabrication of micro ellipse pattern by maskless electrochemical micromachining. *J Manuf Process* 35:700–714. <https://doi.org/10.1016/j.jmapro.2018.09.005>
14. Zhao L, Zhang Y, Bian H, Wang G, Ji L (2022) Investigation of electrochemical dissolution behavior of Ni ( $\gamma$ )/Ni3Al ( $\gamma'$ ) and Co ( $\gamma$ )/Co3Al ( $\gamma'$ ) superalloys in NaNO<sub>3</sub> solution. *Corros Sci* 208:110622. <https://doi.org/10.1016/j.corsci.2022.110622>
15. Wu M, Liu J, He J, Chen X, Guo Z (2020) Fabrication of surface microstructures by mask electrolyte jet machining. *Int J Mach Tool Manu* 148:103471. <https://doi.org/10.1016/j.ijmactools.2019.103471>
16. Chen XL, Zhu JJ, Xu Z, Su GK (2021) Modeling and experimental research on the evolution process of micro through-slit array generated with masked jet electrochemical machining. *J Mater Process Tech* 298:117304. <https://doi.org/10.1016/j.jmatprotec.2021.117304>
17. Zhai K, Du L, Wen Y, Wang S, Cao Q, Zhang X, Liu J (2020) Fabrication of micro pits based on megasonic assisted through-mask electrochemical micromachining. *Ultrasonics* 100:105990. <https://doi.org/10.1016/j.ultras.2019.105990>
18. Kunar S, Bhattacharyya B (2019) Electrochemical micromachining of micro square pattern using reusable masked tool. *Mater Manuf Process* 34(5):487–493. <https://doi.org/10.1080/10426914.2018.1532582>



19. Chen XL, Fan GC, Lin CH, Dong BY, Guo ZN, Fang XL, Qu NS (2020) Investigation on the electrochemical machining of micro groove using masked porous cathode. *J Mater Process Tech* 276:116406. <https://doi.org/10.1016/j.jmatprotec.2019.116406>
20. Zhao C, Ming P, Zhang X, Qin G, Shen J, Yan L et al (2020) Through-mask electrochemical micromachining with reciprocating foamed cathode. *Micromachines* 11(2):188. <https://doi.org/10.3390/mi11020188>
21. Mahata S, Kunar S, Bhattacharyya B (2018) Micro dimple array fabrication by through mask electrochemical micromachining utilizing low-aspect ratio mask. *J Electrochem Soc* 165(3):E129–E137. <https://doi.org/10.1149/2.0521803jes>
22. Patel DS, Agrawal V, Ramkumar J, Jain VK, Singh G (2020) Micro-texturing on free-form surfaces using flexible-electrode through-mask electrochemical micromachining. *J Mater Process Tech* 282:116644. <https://doi.org/10.1016/j.jmatprotec.2020.116644>
23. Zhang X, Qu N, Chen X (2016) Sandwich-like electrochemical micromachining of micro-dimples. *Surf Coat Tech* 302:438–447. <https://doi.org/10.1016/j.surfcoat.2017.01.035>
24. Chen XL, Dong BY, Zhang CY, Wu M, Guo ZN (2018) Jet electrochemical machining of micro dimples with conductive mask. *J Mater Process Tech* 257:101–111. <https://doi.org/10.1016/j.jmatprotec.2018.02.035>

**Publisher's note** Springer Nature remains neutral with regard to jurisdictional claims in published maps and institutional affiliations.

Springer Nature or its licensor (e.g. a society or other partner) holds exclusive rights to this article under a publishing agreement with the author(s) or other rightsholder(s); author self-archiving of the accepted manuscript version of this article is solely governed by the terms of such publishing agreement and applicable law.